

Tumbling of a Brownian particle in an extensional flow

Emmanuel Lance Christopher VI Medillo Plan and Dario Vincenzi

Laboratoire Jean Alexandre Dieudonné, Université Nice Sophia Antipolis, CNRS, UMR 7351, 06108 Nice, France

The phenomenon of tumbling of microscopic objects is commonly associated with shear flows. We address the question of whether tumbling can also occur in stretching-dominated flows. To answer this, we study the dynamics of a semi-flexible trumbbell in a planar extensional velocity field. We show that the trumbbell undergoes a random tumbling-through-folding motion. The probability distribution of long tumbling times is exponential with a time scale exponentially increasing with the Weissenberg number.

I. INTRODUCTION

Various microscopic objects, when immersed in a laminar shear flow, perform a tumbling motion in the plane of the shear. These include anisotropic solid particles [1], flexible and semi-flexible polymers [2–4], vesicles [5], bacteria [6], red blood cells [7] (for related numerical studies, see, e.g., Refs. [8–13]). The tumbling dynamics depends on the nature of the object and on its interaction with the fluid: tumbling may occur only within a restricted range of shear rates, and it can be periodic, chaotic, or random.

Axisymmetric solid particles and elastic dumbbells are among the simplest objects that tumble in shear flows. In a viscous simple shear flow of a Newtonian fluid, a neutrally buoyant axisymmetric particle spends most of the time aligned with the direction of the flow and periodically reverses its orientation [14, 15]. If the axisymmetry of the particle is broken, the tumbling motion may become doubly-periodic or even chaotic [1, 16, 17]. An elastic dumbbell, which consists of two beads joined by a spring, also performs an end-over-end tumbling motion in a shear flow [18–21]. Under the effect of Brownian fluctuations, the reversals occur at random times and are characterised by a transition from the stretched to the coiled state. The distribution of the time intervals separating two reversals has an exponential tail with a time scale that decreases as a power-law of the Weissenberg number (the product of the amplitude of the velocity gradient and the relaxation time of the spring).

Here we address the question of whether tumbling can also exist in stretching-dominated flows and, if so, what the minimal requirements are for a particle to tumble in such flows and how the resulting tumbling motion compares with the analogous motion in a shear flow. The orientational dynamics of an axisymmetric particle or of an elastic dumbbell in a purely extensional velocity field is trivial: such objects indeed simply align with the stretching direction. In order to observe tumbling in an extensional flow, we must consider objects that can bend. The ‘trumbbell’ is one of the simplest semi-flexible objects: It consists of three beads joined by two rigid connectors and of an elastic hinge at the central bead [22] (see also [23]). Owing to its simplicity, the trumbbell was originally used to study the low-frequency dynamics of stiff macromolecules analytically (e.g. [24, 25]). We show that in an extensional flow a trumbbell spends a significant amount of time extended and oriented along the stretching direction of the flow; occasionally, a favourable sequence of Brownian fluctuations make the trumbbell fold, reverse its orientation, and unfold. We examine this tumbling-through-folding dynamics in terms of the stable configurations of the trumbbell and of the associated basins of attraction. The properties of the statistics of the tumbling times are explained by using the large deviations theory. In particular, the analysis of the tumbling statistics reveals a fundamental difference between the tumbling motion of a trumbbell in an extensional flow and the tumbling motion of an elastic dumbbell in a simple shear flow. In the former case, indeed, the mean time that separates two reversals grows with the Weissenberg number, and the growth is exponential.

Section II describes the trumbell and specifies its configuration in terms of angular variables. Section III examines the stationary statistics of the configuration of a trumbell in a two-dimensional extensional flow. Section IV analyses the tumbling motion and its statistical properties; analogous results in three dimensions are also presented. Finally, conclusions are drawn in § V.

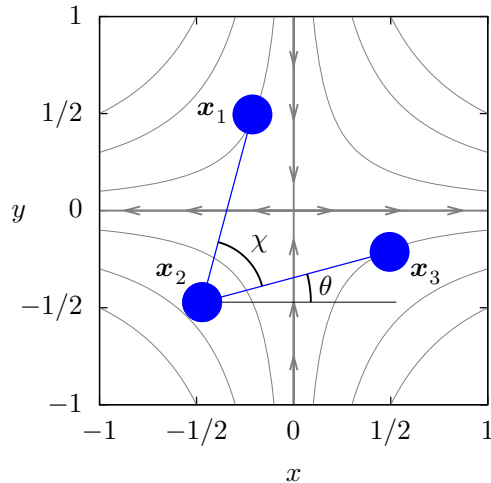


FIG. 1: A trumbbell in the frame of reference of its centre of mass. The origin coincides with the centre of mass. The flow is extensional (streamlines shown in gray) with stretching in the x direction and compression in the y direction. (Online version in colour.)

II. THE TRUMBELL

A trumbbell consists of three identical beads located at \mathbf{x}_ν ($\nu = 1, 2, 3$) and joined by two inertialess rods of length ℓ (see figure 1)*. The internal angle between the rods is denoted by χ ; since we distinguish the two configurations obtained by interchanging \mathbf{x}_1 and \mathbf{x}_3 , χ varies between 0 and 2π . When $\chi = 0, 2\pi$ the trumbbell is folded; when $\chi = \pi$ it is fully extended. A restoring force is imposed so that the trumbbell unfolds towards an equilibrium at $\chi = \pi$. This force is described by the harmonic potential $\phi(\chi) = \mu(\chi - \pi)^2/2$ and models the resistance of the trumbbell to bend.

The trumbbell is advected by a linear velocity field $\mathbf{u}(\mathbf{x}, t)$, in which each bead experiences Stokes' drag with drag coefficient ζ . The fluid is Newtonian. The beads are assumed to be sufficiently small to experience Brownian fluctuations. Furthermore, the inertia of the beads and the hydrodynamic interactions between them are neglected. It is also assumed that the trumbbell does not modify the flow.

The centre of mass of the trumbbell, $\mathbf{x}_{\text{CM}} = (\mathbf{x}_1 + \mathbf{x}_2 + \mathbf{x}_3)/3$, moves according to the equation: $\dot{\mathbf{x}}_{\text{CM}} = \mathbf{u}(\mathbf{x}_{\text{CM}}, t) + \sqrt{2\zeta k_B T/3} \hat{\boldsymbol{\eta}}(t)$, where k_B is the Boltzmann constant, T is temperature, and $\hat{\boldsymbol{\eta}}(t)$ is white noise (see the appendix). In the reference frame of \mathbf{x}_{CM} , the configuration of the trumbbell can be described by $2(d-1)$ angular coordinates \mathbf{q} , where d is the dimension of the flow [22]. The statistics of the configuration of the trumbbell at a time t is specified by the probability density function (p.d.f.) $\psi(\mathbf{q}; t)$, which is normalised as $\int \psi(\mathbf{q}; t) d\mathbf{q} = 1$ and satisfies the following diffusion equation [22] (see also Ref. [23] for the derivation):

$$\frac{\partial \psi}{\partial t} = -\frac{\partial}{\partial q^i} \left\{ \mathcal{G}^{ij} \left[\left(\kappa^{kl}(t) r_\nu^l \frac{\partial r_\nu^k}{\partial q^j} - \frac{1}{\zeta} \frac{\partial \phi}{\partial q^j} \right) \psi - \frac{k_B T}{\zeta} \sqrt{h} \frac{\partial}{\partial q^j} \left(\frac{\psi}{\sqrt{h}} \right) \right] \right\}, \quad (1)$$

where $\kappa^{kl}(t) = \partial^l \mathbf{u}^k(t)$ is the velocity gradient evaluated at \mathbf{x}_{CM} , $\mathbf{r}_\nu = \mathbf{x}_\nu - \mathbf{x}_{\text{CM}}$ are the separation vectors describing the location of the beads with respect to \mathbf{x}_{CM} , $h = \det(\mathcal{H})$ with $\mathcal{H}^{ij} = \sum_{\nu, k} \frac{\partial r_\nu^k}{\partial q^i} \frac{\partial r_\nu^k}{\partial q^j}$, and $\mathcal{G} = \mathcal{H}^{-1}$. Summation over repeated indices is implied in (1). Note that in a linear flow the orientational dynamics of the trumbbell only depends on the velocity gradient, which is spatially uniform (see also the evolution equations for the configuration of the trumbbell in the appendix). The internal configuration of the trumbbell is therefore decoupled from the position of the centre of mass. This implies that the statistics of \mathbf{q} is independent of \mathbf{x}_{CM} ; hence, without any loss of generality, we study the dynamics of the trumbbell in the frame of reference that is translated with the centre of mass.

To simplify the analysis, we assume that the trumbbell is immersed in a thin layer of fluid and we restrict our attention to $d = 2$. The case of a planar three-dimensional flow will be discussed at the end of § IV. In two

* Throughout the paper vectors are written in bold; calligraphic letters denote tensors.

dimensions, we choose $\mathbf{q} = (\theta, \chi)$, where $0 \leq \theta < 2\pi$ is the angle that the vector $\mathbf{x}_3 - \mathbf{x}_2$ makes with the x -axis; θ gives the orientation of the trumbell in the plane. The vectors \mathbf{r}_ν can then be expressed in terms of θ and χ as

$$\begin{aligned}\mathbf{r}_1 &= \ell (2 \cos(\theta + \chi) - \cos(\theta), 2 \sin(\theta + \chi) - \sin(\theta)) / 3, \\ \mathbf{r}_2 &= -\ell (\cos(\theta + \chi) + \cos(\theta), \sin(\theta + \chi) + \sin(\theta)) / 3, \\ \mathbf{r}_3 &= \ell (2 \cos(\theta) - \cos(\theta + \chi), 2 \sin(\theta) - \sin(\theta + \chi)) / 3.\end{aligned}$$

We also have $h = \ell^4(4 - \cos^2 \chi)/9$ and

$$\mathcal{G} = \ell^{-2} \begin{pmatrix} \frac{6}{4 - \cos^2 \chi} & -\frac{3}{2 + \cos \chi} \\ -\frac{3}{2 + \cos \chi} & \frac{6}{2 + \cos \chi} \end{pmatrix}.$$

Equation (1) can then be rewritten as a Fokker–Planck equation in two variables:

$$\partial_t \psi = -\partial_\theta (V_\theta \psi) - \partial_\chi (V_\chi \psi) + \frac{1}{2} \partial_\theta^2 (D_{\theta\theta} \psi) + \partial_\theta \partial_\chi (D_{\theta\chi} \psi) + \frac{1}{2} \partial_\chi^2 (D_{\chi\chi} \psi), \quad (2)$$

where

$$D_{\theta\theta} = \frac{12k_B T}{\zeta \ell^2 (4 - \cos^2 \chi)}, \quad D_{\theta\chi} = -\frac{6k_B T}{\zeta \ell^2 (2 + \cos \chi)}, \quad D_{\chi\chi} = \frac{12k_B T}{\zeta \ell^2 (2 + \cos \chi)}$$

and

$$\begin{aligned}V_\theta &= -\frac{6k_B T \sin \chi}{\zeta \ell^2 (2 - \cos \chi)(2 + \cos \chi)^2} - \frac{3\mu(\pi - \chi)}{\zeta \ell^2 (2 + \cos \chi)} - \\ &\quad \frac{1}{4 - \cos^2 \chi} \{ [2 \sin \chi \cos^2(\theta + \chi) + \cos \theta (4 \sin \theta - \cos \chi \sin(\theta + \chi))] \kappa^{11}(t) + \\ &\quad [2 \cos \chi \sin^2(\theta + \chi) - \sin \theta (2 + \cos \chi) \sin(\theta + \chi) + 4 \sin^2 \theta] \kappa^{12}(t) + \\ &\quad [-2 \cos \chi \cos^2(\theta + \chi) + \cos \theta (2 + \cos \chi) \cos(\theta + \chi) - 4 \cos^2 \theta] \kappa^{21}(t) + \\ &\quad [2 \cos \theta (\sin(\theta + \chi) - 2 \sin \theta) + \cos \chi (\sin \theta \cos(\theta + \chi) - \sin(2(\theta + \chi)))] \kappa^{22}(t) \}, \\ V_\chi &= \frac{12k_B T \sin \chi}{\zeta \ell^2 (2 - \cos \chi)(2 + \cos \chi)^2} + \frac{6\mu(\pi - \chi)}{\zeta \ell^2 (2 + \cos \chi)} + \frac{\sin \chi}{2 + \cos \chi} \{ [1 - 2 \cos(2\theta + \chi)] \kappa^{11}(t) - \\ &\quad 2 \sin(2\theta + \chi) [\kappa^{12}(t) + \kappa^{21}(t)] + [1 + 2 \cos(2\theta + \chi)] \kappa^{22}(t) \}.\end{aligned}$$

The Fokker–Planck equation (2) is equivalent to the following system of Itô stochastic differential equations:

$$\begin{aligned}\dot{\theta}(t) &= V_\theta + \sqrt{D_{\theta\theta}} \xi_\theta(t), \\ \dot{\chi}(t) &= V_\chi + \frac{D_{\theta\chi}}{\sqrt{D_{\theta\theta}}} \xi_\theta(t) + \sqrt{D_{\chi\chi} - \frac{D_{\theta\chi}^2}{D_{\theta\theta}}} \xi_\chi(t),\end{aligned} \quad (3)$$

where $\xi_\theta(t)$ and $\xi_\chi(t)$ are independent white noises. Note that in (3) $D_{\chi\chi} - D_{\theta\chi}^2/D_{\theta\theta} = 3k_B T/\zeta \ell^2$.

III. STATIONARY STATISTICS OF THE CONFIGURATION

By rescaling time in system (3), it is possible to formulate the equations in terms of two dimensionless parameters: the stiffness parameter $Z = \mu/k_B T$ and the Weissenberg number $Wi = \gamma \zeta \ell^2/\mu$, where γ is the magnitude of the velocity gradient. The former expresses the relative intensity of the restoring force to that of Brownian noise, whereas the latter compares the strengths of the flow and of the restoring force. In addition, we introduce the Péclet number $Pe = \gamma \zeta \ell^2/k_B T = Z Wi$, which is the relative intensity of the flow to Brownian noise.

Consider a two-dimensional extensional flow $\mathbf{u}(x, y) = \gamma(x, -y)$, $\gamma > 0$, which consists of a stretching direction x and a compressing direction y (figure 1)[†]. For this flow, the stationary p.d.f. of θ and χ takes the form $\psi_{\text{st}}(\theta, \chi) =$

[†] As noted in § 2, our study is not restricted to the case in which the centre of mass stays fixed at the stagnation point of the extensional flow, but it is conducted in the frame of reference of the centre of mass and takes advantage of the fact that the statistics of the configuration is independent of \mathbf{x}_{CM} .

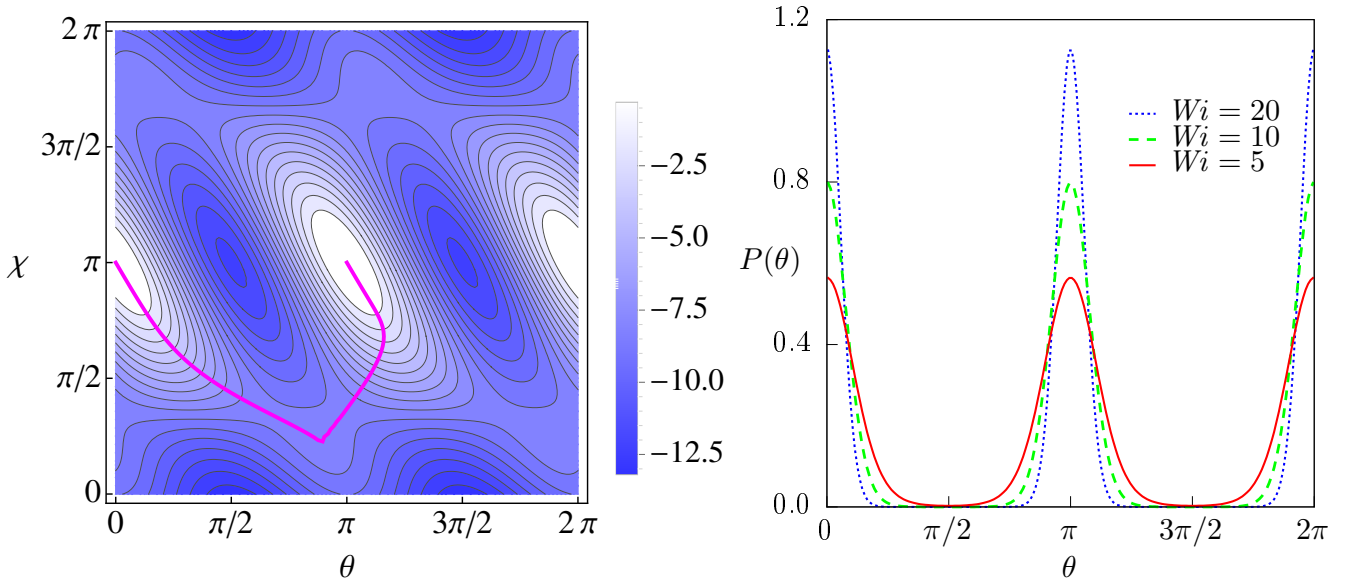


FIG. 2: Left: Contourplot of $\ln \psi_{st}(\theta, \chi)$ for $Z = 1$ and $Wi = 6$. One minimum energy path (see § IV) connecting (π, π) and $(0, \pi)$ is drawn with a solid magenta curve. Right: The marginal p.d.f. of θ for $Z = 1$ and $Wi = 5$ (red, solid), $Wi = 10$ (green, dashed), and $Wi = 20$ (blue, dotted). (Online version in colour.)

$N\sqrt{h} \exp[(\Phi - \phi)/(k_B T)]$ with $\Phi = (\zeta/2) \sum \kappa^{ij} r_\nu^i r_\nu^j$ [22]; its explicit expression is:

$$\psi_{st}(\theta, \chi) = N\sqrt{4 - \cos^2 \chi} \exp \left[\frac{Z Wi (2 \cos \chi - 1) \cos(2\theta + \chi)}{3} - \frac{Z(\pi - \chi)^2}{2} \right], \quad (4)$$

where N is a normalization constant. The contour plot of $\ln \psi_{st}(\theta, \chi)$ is shown in figure 2 (left) for representative values of Z and Wi . It is easily shown that the maxima of $\psi_{st}(\theta, \chi)$ are located at $P_\pi : (\theta = n\pi, \chi = \pi)$, where n is an integer. Hence, the trumbbell spends most of the time in an extended configuration and oriented in the stretching direction of the flow. The peaks at P_π become narrower as Wi increases, showing stronger preference for these configurations (see the marginal p.d.f. of θ , $P(\theta)$ in figure 2, right). Also note that these peaks are not symmetrically distributed around P_π .

To understand the behaviour of $\psi_{st}(\theta, \chi)$ when the flow is much stronger than both the restoring force and Brownian noise, we set $\mu = 0$ and $k_B T = 0$ in (3), which corresponds to considering the limiting case $Wi = Pe = \infty$. The resulting system is:

$$\begin{aligned} \dot{\theta}(t) &= -\frac{\gamma}{2(4 - \cos^2 \chi)} [7 \sin(2\theta) + 4 \cos(2\theta + \chi) \sin \chi - \sin(2(\theta + \chi))], \\ \dot{\chi}(t) &= -\frac{4\gamma}{2 + \cos \chi} [\sin \chi \cos(2\theta + \chi)]. \end{aligned} \quad (5)$$

The linear stability analysis of this system yields two stable configurations, both aligned with the stretching direction of the flow ($\theta = 0, \pi, 2\pi$). The first stable configuration is the extended one P_π and is characterised by two negative eigenvalues: $\lambda_\pi^{(1)} = -4\gamma, \lambda_\pi^{(2)} = -2\gamma$. The second stable configuration is the folded one $P_0 : (\theta = n\pi, \chi = 0, 2\pi)$ with eigenvalues $\lambda_0^{(1)} = -2\gamma, \lambda_0^{(2)} = -4\gamma/3$. As the velocity gradient γ becomes stronger, both configurations become increasingly stable, since the eigenvalues are proportional to γ . However, the ratio of the most negative eigenvalues of the two configurations is $\lambda_\pi^{(1)}/\lambda_0^{(1)} = 2$; hence the extended configuration P_π is more stable than the folded one P_0 for all γ and is expected to dominate the long-time statistics. This fact can be understood by noting that the velocity of a bead is proportional to its distance from the center of mass, and in the extended configuration P_π the end beads are farther from \mathbf{x}_{CM} than they are in the folded configuration P_0 .

The presence of the two stable configurations is seen in the vector plot of $(\dot{\theta}, \dot{\chi})$ shown in figure 3 (left). As both $\dot{\theta}$ and $\dot{\chi}$ are proportional to γ [see (5)], the geometrical structure of the vector plot does not change with γ . In accordance with the stability analysis of the fixed points of (5), the vectors that lie in the neighbourhood of P_π are larger than those in the neighbourhood of P_0 . Therefore, the presence of Brownian noise allows an easier escape from the basin

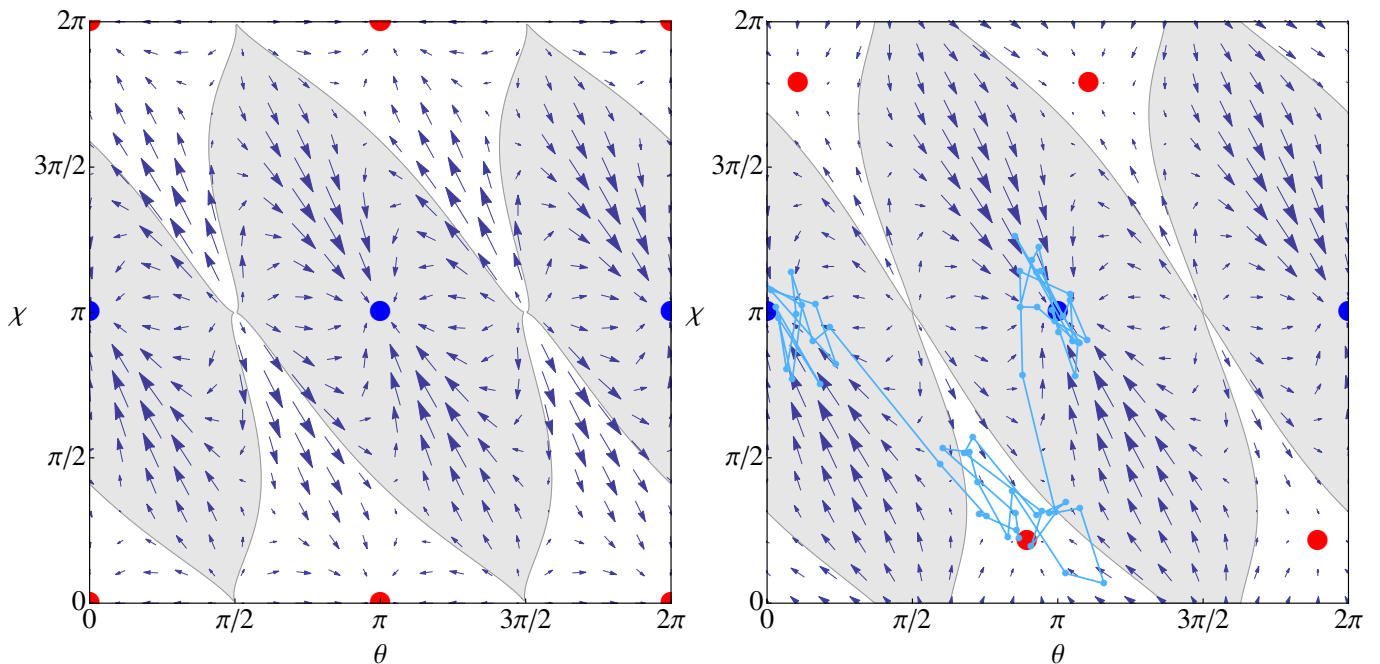


FIG. 3: Left: Vector plot of $\gamma^{-1}(\dot{\theta}, \dot{\chi})$ for $Wi = Pe = \infty$. The size of the arrows are proportional to the magnitude of the vector $\gamma^{-1}(\dot{\theta}, \dot{\chi})$. The basins of attraction of P_π (blue disks) are in gray; those of P_0 (red disks) are in white. Right: Vector plot of $(\dot{\theta}, \dot{\chi})$ for $Z = 1, Wi = 6$. The white areas are now the basins of attraction of P_* (red disks). The light blue curve with markers is a trajectory $(\theta(t), \chi(t))$ corresponding to a tumbling motion from $\theta = \chi = \pi$ to $\theta = 0, \chi = \pi$. (Online version in colour.)

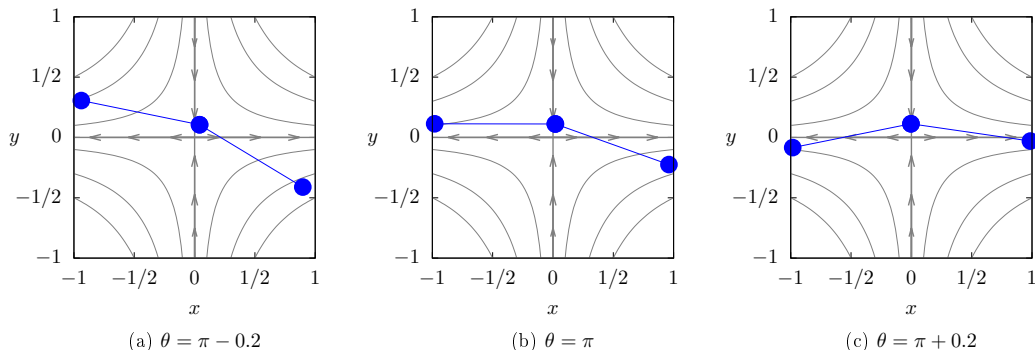


FIG. 4: Three configurations near an extended equilibrium configuration for the same value of $\chi = 2.8$. (Online version in colour.)

of attraction of the folded configuration P_0 than from that of the extended configuration P_π . Conversely, a trumbell in an extended configuration is more likely to remain in the basin of attraction of this configuration, until there is sufficient noise for it to fold. Also note that the basin of attraction of the points P_π is not symmetrically distributed around them, but there is a preferential direction along which the system is more strongly attracted (see figure 3). Consider indeed two configurations with the same value of χ close to π and with θ either slightly less than π or slightly greater than it (see figure 4). It is clear that the latter configuration is more strongly attracted to P_π .

In the presence of restoring potential ($Wi < \infty, Pe = \infty$), the fixed points of system (3) and their stability can be calculated numerically. Only P_π remain stable fixed points; the configurations P_0 are no longer fixed because of the restoring potential. However, if the flow is sufficiently strong ($Wi \gtrsim 4$ for $Z = 1$), there exist stable points $P_* : (\theta_*, \chi_*)$ that approach P_0 as Wi increases (see figures 3, right and figure 5, left). Moreover, the points P_π are more stable than P_* for all γ and as Wi increases, the eigenvalues of P_π and P_* approach the corresponding eigenvalues of the $Wi = \infty$ case (figure 5, right). Finally, the basins of attraction of P_π and P_* have similar structures to those of P_π and P_0

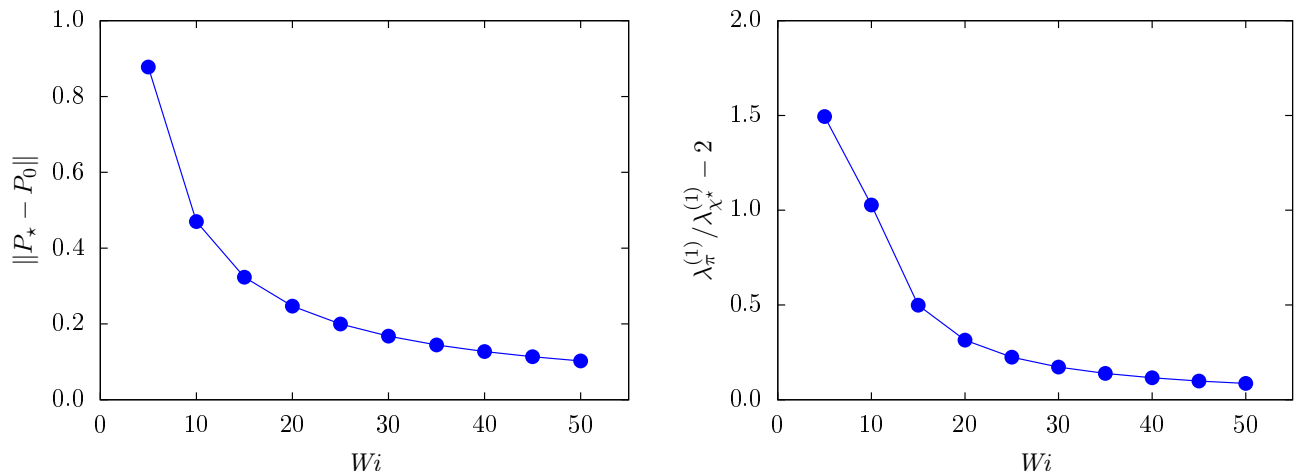


FIG. 5: Left: Distance of a stable fixed point P_* from the nearest P_0 for $Pe = \infty$ as a function of Wi . Right: Ratio of the most negative eigenvalue of P_π to that of P_* subtracted by $\lambda_\pi^{(1)}/\lambda_0^{(1)} = 2$. (Online version in colour.)

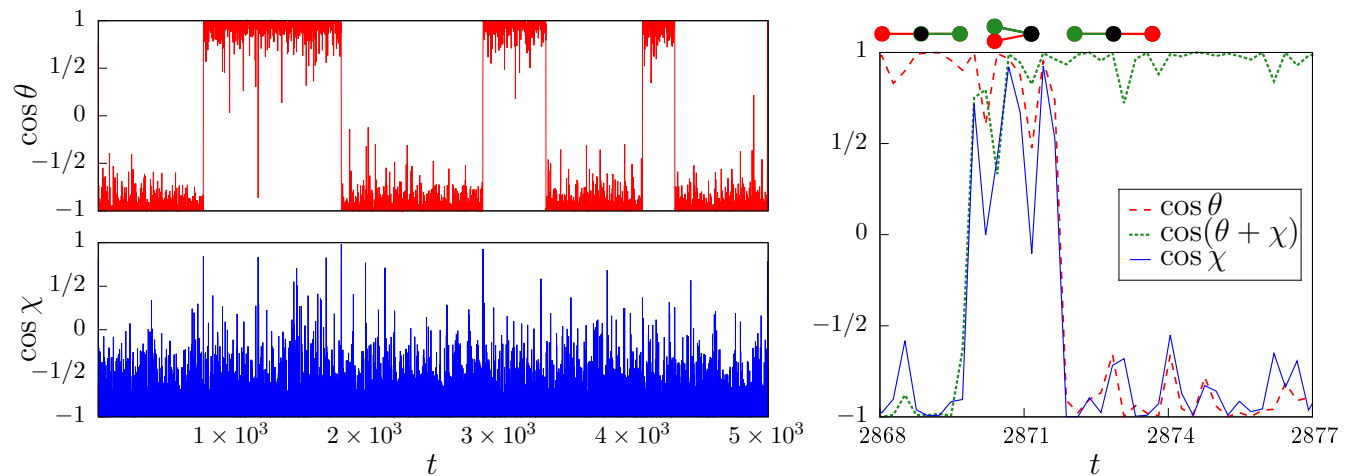


FIG. 6: Time series of $\cos \theta(t)$ (left, top) and $\cos \chi(t)$ (left, bottom) for a two-dimensional extensional flow with $Z = 1$, $Wi = 6$. Right: Zoom of the time series of $\cos \theta$, $\cos \chi$, $\cos(\theta + \chi)$ over a tumbling event. (Online version in colour.)

when Wi is infinite (figure 3, right). These results indicate that the intuition gained from the study of the $Wi = \infty$ case holds true also for $Wi < \infty$. In particular, the stability analysis of the fixed points of the system explains why $\psi_{\text{st}}(\theta, \chi)$ shows high peaks only at the extended configuration P_π and not at the folded configuration. Furthermore, the examination of the basins of attraction of P_π and of the vector field $(\dot{\theta}, \dot{\chi})$ clarifies the shape of these peaks.

IV. TUMBLING DYNAMICS

For sufficiently large Wi , the trumbbell is trapped in the basin of attraction of one of the extended configuration P_π for a long time. However, Brownian fluctuations may occasionally make it tumble between the aligned configuration ($\theta = 0, 2\pi$) and the anti-aligned one ($\theta = \pi$). To investigate this phenomenon, we have performed numerical simulations of (3) by using the Euler–Maruyama scheme with a time step $dt = 10^{-3}$ [26] (we also performed numerical simulations with smaller time steps, which confirmed the accuracy of our results). The inspection of a representative time series of $\cos \theta(t)$ and $\cos \chi(t)$ confirms the aforementioned tumbling dynamics and shows that these reversals are characterised by partial folding (figure 6). A typical trajectory in the (θ, χ) phase space is shown in figure 3 (right). The trumbbell is initially extended and anti-aligned with the stretching direction. A favourable sequence of Brownian

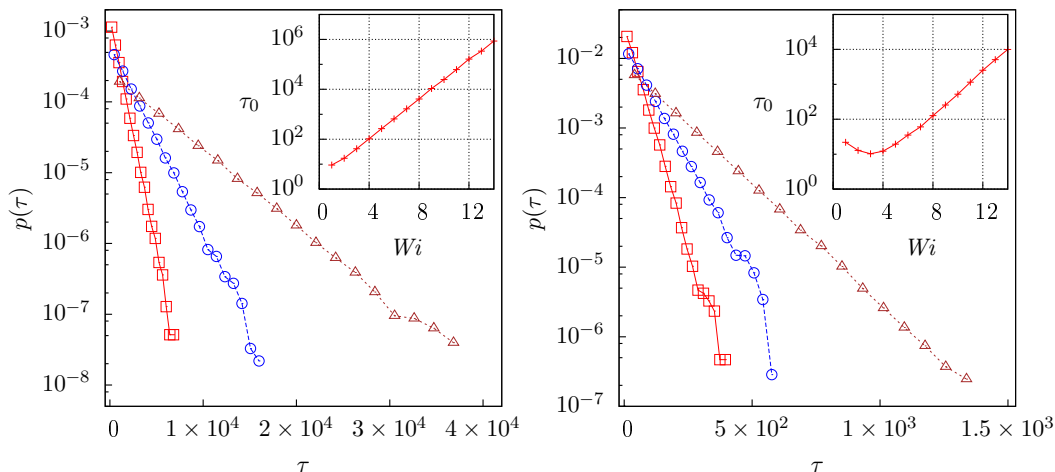


FIG. 7: P.d.f.s of the tumbling time in two dimensions (left) and three dimensions (right) for $Z = 1$ and $Wi = 6$ (red squares), $Wi = 7$ (blue circles), and $Wi = 8$ (brown triangles). The insets show τ_0 as a function of Wi . (Online version in colour.)

fluctuations makes it exit from the initial basin of attraction and pass through that of the folded configuration. The trumbbell then unfolds towards the extended but aligned configuration. The movie included as a supplementary material further illustrates this tumbling-through-folding motion.

Although the trumbbell always folds (possibly not completely) during a tumbling event, there are instances in which folding does not result into a reversal and the trumbbell rapidly unfolds back into the original configuration (see for instance figure 6 at $t \approx 1.2 \times 10^3$). In order to correctly identify a tumbling event, we shall therefore apply the following criterion. Suppose that at time t_1 the trumbbell is sufficiently extended, i.e.

$$|\cos \theta| > 1 - \epsilon, \quad |\cos(\theta + \chi)| > 1 - \epsilon, \quad \cos \theta \cos(\theta + \chi) < 0 \quad (6)$$

for some small ϵ . We shall say that a tumbling occurs at time t_2 if t_2 is the smallest time after t_1 such that (6) is again satisfied and $\cos \theta(t_1) \cos \theta(t_2) < 0$. In our simulations, we set $\epsilon = 0.01$; we have verified that the specific choice of ϵ does not affect the statistical analysis of tumbling, provided the threshold $1 - \epsilon$ is sufficiently close to 1.

The tumbling dynamics described above is not periodic. On the contrary, the time τ separating two tumbling events are distributed randomly. For each different value of Wi , we have collected at least 10^4 tumbling realizations. We find that the p.d.f. of τ has an exponential tail for large τ : $p(\tau) \propto \exp(-\tau/\tau_0)$ for $\tau \gg \tau_0$. Moreover, τ_0 increases exponentially as a function of Wi (figure 7, left). Hence, as the flow becomes stronger, it takes a longer time for a tumbling to occur. The configurations P_π indeed become increasingly stable, and larger Brownian fluctuations are required for the system to escape from the basins of attraction of P_π .

The above properties of $p(\tau)$ can be predicted by using the Freidlin–Wentzell large deviations theory [27] (see also [28]). Indeed, for large values of Wi , tumbling in an extensional flow can be regarded as escaping from an attractor of a stochastic dynamical system in the limit of small noise. The p.d.f. of the exit time thus has an exponential tail and the mean exit time increases exponentially as the amplitude of the noise vanishes. The same theory also predicts the tumbling-through-folding phenomenon. Indeed, the most probable transition paths, or minimum energy paths, that connect two adjacent configurations P_π are parallel to the gradient of the pseudo-potential $V = -\ln \psi_{st}$ [29]. The application of the improved string method to V [30] shows that these minimum energy paths pass through the folded configurations P_* , which are saddle points of V . By way of illustration, a minimum energy path connecting (π, π) and $(0, \pi)$ is given in figure 3 (right).

The analysis so far considers a two-dimensional velocity field. However, in a realistic planar extensional flow, a trumbbell may move outside the plane of the flow. This situation can be described by considering a three-dimensional velocity field $\mathbf{u} = \gamma(x, -y, 0)$. In this case, the trumbbell has four degrees of freedom, which can be described by the internal angle χ and three Euler angles giving the orientation of the particle in space [22, 23]. This formulation, however, is not suitable for numerical simulations because of singularities near to the extended configuration (see the form of the tensor \mathcal{G} in [23], p. 618). To circumvent this difficulty, we introduce the vectors $\boldsymbol{\rho}_1 = \mathbf{x}_1 - \mathbf{x}_2$ and $\boldsymbol{\rho}_3 = \mathbf{x}_3 - \mathbf{x}_2$, which give the orientation of the rods in the frame of reference of the centre of mass. The system of Stratonovich stochastic differential equations that describes the time evolution of $\boldsymbol{\rho}_1$ and $\boldsymbol{\rho}_3$ is derived in the appendix. This system has been solved by using the Euler–Heun method with $dt = 10^{-3}$ [26]. When Wi is sufficiently high, the trumbbell is observed to be predominantly in the extended configuration $\chi = \pi$ with the separation vectors aligned or anti-aligned with the stretching direction of the flow. At random times, the trumbbell folds and reverses its orientation,

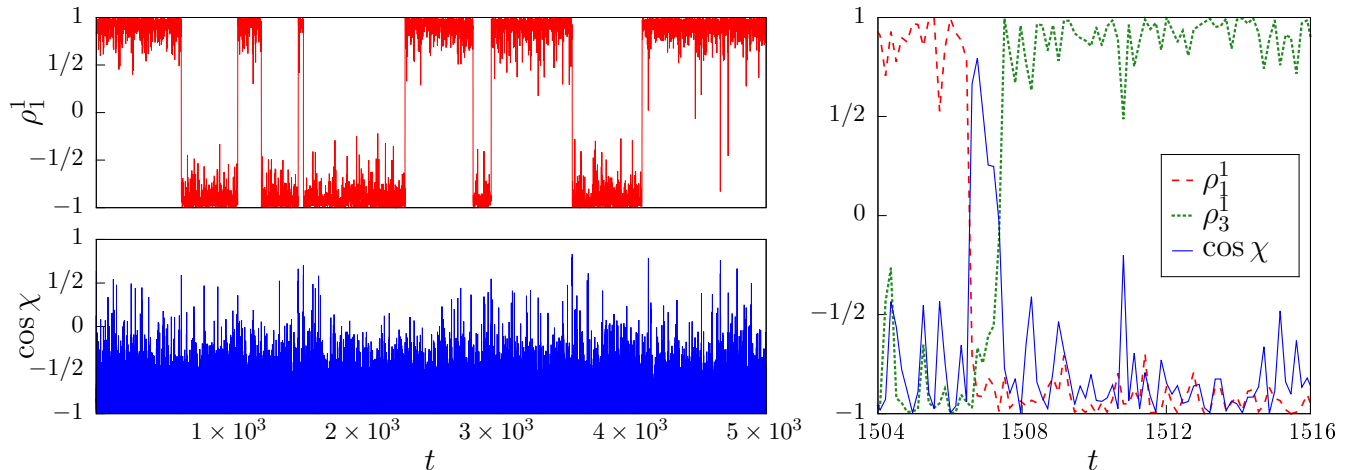


FIG. 8: Time series of $\rho_1^1(t)$ (left, top) and $\cos \chi(t)$ (left, bottom) for a three-dimensional planar extensional flow with $Z = 1$, $Wi = 10$. Right: Zoom of the time series of $\rho_1^1, \rho_3^1, \cos \chi$ over a tumbling event. (Online version in colour.)

with a dynamics similar to that observed in two dimensions. A time series showing $\cos \chi$ and the first component of $\boldsymbol{\rho}_1$ is shown in figure 8. The tumbling events can be identified as before by replacing $\cos \theta, \cos(\theta + \chi)$ with the first components of $\boldsymbol{\rho}_1, \boldsymbol{\rho}_3$, respectively. The p.d.f. of the tumbling time is again exponential for long times with a time scale increasing exponentially with Wi (figure 7, right). The tumbling statistics, therefore, shows properties similar to those found in a purely two dimensional flow. For the same values of Wi , the mean tumbling time is however significantly shorter than in two dimensions. This fact is attributed to the increased dimensionality of the system, which makes it easier for the trumbbell to escape from the aligned or anti-aligned configuration. For the same reason, the asymptotic exponential behavior of τ_0 is observed at larger Wi compared to the two-dimensional case.

V. CONCLUSION

The phenomenon of tumbling is commonly associated with shear flows. The simplest objects that perform end-over-end tumbling in a simple shear, viz. axisymmetric solid particles and the dumbbell, exhibit a trivial orientational dynamics in an extensional flow and do not tumble. We have shown that, in contrast, a rich dynamics is obtained by considering one of the most elementary semi-flexible objects, namely the trumbbell. The mere consideration of one bending mode indeed yields a random end-over-end tumbling motion with exponentially distributed tumbling times. While it is well known that several microscopic objects tumble in a shear flow, to the best of our knowledge tumbling had not been observed in an extensional flow before. Moreover, we find a fundamental qualitative difference between the tumbling motion in an extensional flow and the analogous motion in a shear flow. In the latter case, the typical tumbling time decreases as a power law of Wi ; in the former case, it increases exponentially as Wi increases. This difference is a consequence of the fact that the configurations aligned with the flow are stable in an extensional flow, whereas they are unstable in a shear flow.

We have also shown that, in an extensional flow, a trumbbell reverses its orientation by folding and then extending again in the opposite direction. This dynamics is reminiscent of the buckling instability of a fiber near to a hyperbolic point [31]. Nevertheless, the tumbling motion described here is triggered by Brownian fluctuations that bend the trumbbell, whereas the buckling instability of a fiber results from its internal dynamics and does not necessarily require Brownian fluctuations.

The simplicity of the trumbbell model has allowed us to study its tumbling motion in detail and to relate this phenomenon to the properties of the stable configurations of the trumbbell and to the structure of the corresponding basins of attraction. In our study, we have focused on the most elementary version of the trumbbell model. In particular, we have disregarded hydrodynamic and excluded volume interactions between the beads. If the size of the beads is sufficiently smaller than their mutual separations, the inclusion of such interactions into the model would somewhat modify the stable folded configuration but not the essential structure of the phase space of the system. Therefore, although a more accurate description of the trumbbell would require taking into account hydrodynamic and excluded volume interactions [32, 33], we do not expect these interactions to alter the essential properties of the

tumbling dynamics, as long as the size of the beads is small compared to their mutual separations.

Acknowledgments

This work was supported in part by the EU COST Action MP 1305 ‘Flowing Matter’. ELCMP acknowledges the support of EACEA through the Erasmus Mundus Mobility with Asia program. The authors are grateful to A. Ali, F. Delarue, S. Musacchio and S. S. Ray for useful discussions.

Appendix A: Equations of motion of the trumbbell

In this appendix, we derive an alternative formulation of the internal dynamics of the trumbbell that is suitable for numerical simulations in three dimensions. In the reference frame of \mathbf{x}_{CM} , the configuration of a trumbbell can be described by using the vectors $\boldsymbol{\rho}_1 = \mathbf{x}_1 - \mathbf{x}_2$ and $\boldsymbol{\rho}_3 = \mathbf{x}_3 - \mathbf{x}_2$. The position vectors of the beads satisfy:

$$m\ddot{\mathbf{x}}_\nu = -\zeta[\dot{\mathbf{x}}_\nu - \mathbf{u}(\mathbf{x}_\nu, t)] + \mathbf{t}_\nu + \mathbf{f}_\nu + \sqrt{D}\boldsymbol{\eta}_\nu(t), \quad \nu = 1, 2, 3, \quad (\text{A1})$$

where m is the mass of each bead, $D = 2\zeta k_B T$ and $\boldsymbol{\eta}_\nu(t)$ are independent d -dimensional white noises. The restoring forces \mathbf{f}_ν take the form $\mathbf{f}_1 = \mu_\chi(\hat{\boldsymbol{\rho}}_1 \cot \chi - \hat{\boldsymbol{\rho}}_3 \csc \chi)$, $\mathbf{f}_3 = \mu_\chi(\hat{\boldsymbol{\rho}}_3 \cot \chi - \hat{\boldsymbol{\rho}}_1 \csc \chi)$ and $\mathbf{f}_2 = -(\mathbf{f}_1 + \mathbf{f}_3)$ with $\mu_\chi = \mu(\pi - \chi)/\ell$ [32]. The tensions \mathbf{t}_ν keep the distances between the beads constant. The terms on the r.h.s. of (A1) describe Stokes’ drag, the rigidity of the rods, the resistance of the particle to bend, and Brownian noise, respectively. Neglecting inertial effects yields:

$$\dot{\mathbf{x}}_\nu = \mathbf{u}(\mathbf{x}_\nu, t) + \frac{1}{\zeta} [\mathbf{t}_\nu + \mathbf{f}_\nu + \sqrt{D}\boldsymbol{\eta}_\nu(t)], \quad \nu = 1, 2, 3. \quad (\text{A2})$$

By using the linearity of the velocity field, we obtain:

$$\dot{\mathbf{x}}_{\text{CM}} = \mathbf{u}(\mathbf{x}_{\text{CM}}, t) + \sqrt{\frac{D}{3}}\hat{\boldsymbol{\eta}}(t), \quad (\text{A3})$$

where $\hat{\boldsymbol{\eta}}(t)$ is white noise, and

$$\begin{aligned} \dot{\boldsymbol{\rho}}_1 &= \boldsymbol{\rho}_1 \cdot \nabla \mathbf{u} + \frac{1}{\zeta} (2\mathbf{t}_1 + \mathbf{t}_3) + \frac{1}{\zeta} (2\mathbf{f}_1 + \mathbf{f}_3) + \Gamma \tilde{\boldsymbol{\eta}}_1, \\ \dot{\boldsymbol{\rho}}_3 &= \boldsymbol{\rho}_3 \cdot \nabla \mathbf{u} + \frac{1}{\zeta} (2\mathbf{t}_3 + \mathbf{t}_1) + \frac{1}{\zeta} (2\mathbf{f}_3 + \mathbf{f}_1) + \Gamma \tilde{\boldsymbol{\eta}}_3, \end{aligned} \quad (\text{A4})$$

where $\Gamma = \sqrt{2D}/\zeta$ and $\tilde{\boldsymbol{\eta}}_i = [\boldsymbol{\eta}_i(t) - \boldsymbol{\eta}_i(t')]/\sqrt{2}$ with $\langle \tilde{\boldsymbol{\eta}}_i(t) \rangle = 0$ and $\langle \tilde{\eta}_i^\alpha(t) \tilde{\eta}_i^\beta(t') \rangle = \delta^{\alpha\beta} \delta(t - t')$, $i = 1, 3$. We impose the rigidity constraints $d|\boldsymbol{\rho}_i|^2/dt = 0$ to obtain:

$$\boldsymbol{\rho}_i \circ \dot{\boldsymbol{\rho}}_i = 0, \quad (\text{A5})$$

where the symbol ‘ \circ ’ indicates that the dot products involving the noise terms are understood in the Stratonovich sense [26]. Equation (A5) may now be used to calculate the tensions:

$$\begin{aligned} \mathbf{t}_1 &= -\zeta c_\chi [2\sigma_1 - \sigma_3 \cos \chi - \tilde{\mu}_\chi + 2\Gamma(\hat{\boldsymbol{\rho}}_1 \circ \tilde{\boldsymbol{\eta}}_1) - \Gamma \cos \chi (\hat{\boldsymbol{\rho}}_3 \circ \tilde{\boldsymbol{\eta}}_3)] \hat{\boldsymbol{\rho}}_1, \\ \mathbf{t}_2 &= -(\mathbf{t}_1 + \mathbf{t}_3), \\ \mathbf{t}_3 &= -\zeta c_\chi [2\sigma_3 - \sigma_1 \cos \chi - \tilde{\mu}_\chi + 2\Gamma(\hat{\boldsymbol{\rho}}_3 \circ \tilde{\boldsymbol{\eta}}_3) - \Gamma \cos \chi (\hat{\boldsymbol{\rho}}_1 \circ \tilde{\boldsymbol{\eta}}_1)] \hat{\boldsymbol{\rho}}_3, \end{aligned} \quad (\text{A6})$$

where $\sigma_i = \sum_{\alpha, \beta} \ell \hat{\rho}_i^\alpha \partial^\alpha u^\beta \hat{\rho}_i^\beta$ with $\hat{\boldsymbol{\rho}}_i = \boldsymbol{\rho}_i/|\boldsymbol{\rho}_i|$, $c_\chi = (4 - \cos^2 \chi)^{-1}$, and $\tilde{\mu}_\chi = \zeta^{-1} \mu_\chi \sin \chi (2 - \cos \chi)$. By substituting (A6) into (A4), we obtain the system:

$$\begin{aligned} \dot{\boldsymbol{\rho}}_1 &= \mathbf{A}_1 + \mathcal{B}_{11} \circ \tilde{\boldsymbol{\eta}}_1(t) + \mathcal{B}_{13} \circ \tilde{\boldsymbol{\eta}}_3(t), \\ \dot{\boldsymbol{\rho}}_3 &= \mathbf{A}_3 + \mathcal{B}_{31} \circ \tilde{\boldsymbol{\eta}}_1(t) + \mathcal{B}_{33} \circ \tilde{\boldsymbol{\eta}}_3(t). \end{aligned} \quad (\text{A7})$$

The explicit forms of the vectors $\mathbf{A}_1, \mathbf{A}_3$ are:

$$\mathbf{A}_1 = \boldsymbol{\rho}_1 \cdot \nabla \mathbf{u} - 2c_\chi [2\sigma_1 - \sigma_3 \cos \chi - \tilde{\mu}_\chi] \hat{\boldsymbol{\rho}}_1 - c_\chi [2\sigma_3 - \sigma_1 \cos \chi - \tilde{\mu}_\chi] \hat{\boldsymbol{\rho}}_3 + \frac{1}{\zeta} (2\mathbf{f}_1 + \mathbf{f}_3),$$

$$\mathbf{A}_3 = \boldsymbol{\rho}_3 \cdot \nabla \mathbf{u} - 2c_\chi [2\sigma_3 - \sigma_1 \cos \chi - \tilde{\mu}_\chi] \hat{\boldsymbol{\rho}}_3 - c_\chi [2\sigma_1 - \sigma_3 \cos \chi - \tilde{\mu}_\chi] \hat{\boldsymbol{\rho}}_1 + \frac{1}{\zeta} (2\mathbf{f}_3 + \mathbf{f}_1),$$

and the matrix-valued coefficients of the noises are

$$\begin{aligned} \mathcal{B}_{11} &= \Gamma [\mathcal{I} + c_\chi (\hat{\boldsymbol{\rho}}_3 \cos \chi - 4\hat{\boldsymbol{\rho}}_1) \otimes \hat{\boldsymbol{\rho}}_1], \\ \mathcal{B}_{13} &= 2\Gamma c_\chi (\hat{\boldsymbol{\rho}}_1 \cos \chi - \hat{\boldsymbol{\rho}}_3) \otimes \hat{\boldsymbol{\rho}}_3, \\ \mathcal{B}_{31} &= 2\Gamma c_\chi (\hat{\boldsymbol{\rho}}_3 \cos \chi - \hat{\boldsymbol{\rho}}_1) \otimes \hat{\boldsymbol{\rho}}_1, \\ \mathcal{B}_{33} &= \Gamma [\mathcal{I} + c_\chi (\hat{\boldsymbol{\rho}}_1 \cos \chi - 4\hat{\boldsymbol{\rho}}_3) \otimes \hat{\boldsymbol{\rho}}_3], \end{aligned}$$

where \mathcal{I} is the identity matrix and \otimes denotes the tensor product. Equations (A7) can be shown to be statistically equivalent to (1). The angle χ can be obtained from $\boldsymbol{\rho}_1 \cdot \boldsymbol{\rho}_3 = \ell^2 \cos \chi$. The above formulation holds both for $d = 2$ and for $d = 3$.

-
- [1] Einarsson J, Mihiretie BM, Laas A, Ankardal S, Angilella JR, Hanstorp D, Mehlig B. 2016. Tumbling of asymmetric microrods in a microchannel flow. *Phys. Fluids* **28**, 013302.
- [2] Schroeder CM, Teixeira RE, Shaqfeh ESG, Chu S. 2005. Characteristic periodic motion of polymers in shear flow. *Phys. Rev. Lett.* **95**, 018301.
- [3] Gerashchenko S, Steinberg V. 2006. Statistics of tumbling of a single polymer molecule in shear flow. *Phys. Rev. Lett.* **96**, 038304.
- [4] Harasim M, Wunderlich B, Peleg O, Kröger M, Bausch AR. 2013. Direct observation of the dynamics of semiflexible polymers in shear flow. *Phys. Rev. Lett.* **110**, 108302.
- [5] Kantsler C, Steinberg V. 2006. Transition to tumbling and two regimes of tumbling motion of a vesicle in shear flow. *Phys. Rev. Lett.* **96**, 036001.
- [6] Kaya T, Koser H. 2009. Characterization of hydrodynamic surface interactions of *Escherichia coli* cell bodies in shear flow. *Phys. Rev. Lett.* **103**, 138103.
- [7] Dupire J, Socol M, Viallat A. 2012. Full dynamics of a red blood cell in shear flow. *Proc. Natl Acad. Sci.* **109**, 20808–20813.
- [8] Biben, T, Misbah, C. 2003. Tumbling of vesicles under shear flow within an advected-field approach. *Phys. Rev. E* **67**, 031908.
- [9] Biben, T, Kassner, K, Misbah, C. 2005. Phase-field approach to three-dimensional vesicle dynamics. *Phys. Rev. E* **72**, 041921.
- [10] Young, YN, Shelley, SJ. 2007. Stretch-coil transition and transport of fibers in cellular flows. *Phys. Rev. Lett.* **99**, 058303.
- [11] Huang, CC, Sutmann, G, Gompper, G, Winkler, RG. 2011. Tumbling of polymers in semidilute solution under shear flow. *Europhys. Lett.* **93**, 54004.
- [12] Walter, J, Salsac, AV, Barthès-Biesel, D. 2011. Ellipsoidal capsules in simple shear flow: prolate versus oblate initial shapes. *J. Fluid Mech.* **676**, 318–347.
- [13] Sinha, K, Graham, MD. 2015. Dynamics of a single red blood cell in simple shear flow. *Phys. Rev. E* **92**, 042710.
- [14] Jeffery GB. 1922. The motion of ellipsoidal particles immersed in a viscous fluid. *Proc. R. Soc. Lond. A* **102**, 161–179.
- [15] Bretherton FP. 1962. The motion of rigid particles in a shear flow at low Reynolds number. *J. Fluid Mech.* **14**, 284–304.
- [16] Hinch EJ, Leal LG. 1979. Rotation of small non-axisymmetric particles in a simple shear flow. *J. Fluid Mech.* **92**, 591–608.
- [17] Yarin AL, Gottlieb O, Roisman IV. 1997. Chaotic rotation of triaxial ellipsoids in simple shear flow. *J. Fluid Mech.* **340**, 83–100.
- [18] Celani A, Puliafito A, Turitsyn K. 2005. Polymers in linear shear flow: A numerical study. *Europhys. Lett.* **70**, 464–470.
- [19] Chertkov M, Kolokolov I, Lebedev V, Turitsyn K. 2005. Polymer statistics in a random flow with mean shear. *J. Fluid Mech.* **531**, 251–260.
- [20] Puliafito A, Turitsyn K. 2005. Numerical study of polymer tumbling in linear shear flows. *Physica D* **211**, 9–22.
- [21] Turitsyn KS. 2007. Polymer dynamics in chaotic flows with a strong shear component. *J. Expl Theor. Phys.* **105**, 3, 655–664.
- [22] Hassager O. 1974. Kinetic theory and rheology of bead-rod models for macromolecular solutions. *J. Chem. Phys.* **60**, 5, 2111–2124.
- [23] Bird RB, Curtiss CFC, Armstrong RC, Hassager O. 1987. *Dynamics of Polymeric Liquids* vol. II. Wiley.
- [24] Roitman DB. 1987. The elastic trumbbell model for dynamics of stiff chains. *Lecture Notes Phys.* **293**, 192–207.
- [25] Garcia de la Torre J. 1994. Hydrodynamics of segmentally flexible macromolecules. *Eur. Biophys. J.* **23**, 307–322.
- [26] Kloeden PE, Platen E. 1999. *Numerical Solution of Stochastic Differential Equations*. Springer.
- [27] Freidlin MI, Wentzell AD. 2012. *Random Perturbations of Dynamical Systems*. Springer.
- [28] Touchette H. 2009. The large deviation approach to statistical mechanics. *Phys. Rep.* **478**, 1–69.
- [29] E W, Vanden-Eijnden E. 2010. Transition-path theory and path-finding algorithms for the study of rare events. *Annu. Rev. Phys. Chem.* **61**, 3941–420.
- [30] E W, Ren W, Vanden-Eijnden E. 2007. Simplified and improved string method for computing the minimum energy paths in barrier-crossing events. *J. Chem. Phys.* **126**, 164103.

- [31] Lindner A, Shelley M. 2016. Elastic fibers in flows. In *Fluid-Structure Interactions in Low Reynolds-Number Flows* (eds. C. Duprat and H. Stone), pp. 168–192, Royal Society of Chemistry.
- [32] Diaz, FG, Garcia de la Torre J. 1988. Simulation of the rotational Brownian dynamics of a simple segmentally flexible model: The elastic trumbbell *J. Chem. Phys.* **88**, 7698–7705.
- [33] Lewis, RJ, Allison, SA, Eden, D, Pecora, R. 1988. Brownian dynamics simulations of a three-subunit and a ten-subunit worm-like chain: Comparison of results with trumbell theory and with experimental results from DNA. *J. Chem. Phys.* **89**, 2490–2503.